Materials & Design 216 (2022) 110582

Contents lists available at ScienceDirect

Materials & Design

journal homepage: www.elsevier.com/locate/matdes

Investigation of polycaprolactone for bone tissue engineering scaffolds: *In vitro* degradation and biological studies

Yanhao Hou [a,1], Weiguang Wang [a,1,*], Paulo Bartolo [a,b,*]

[a] Department of Mechanical, Aerospace and Civil Engineering, School of Engineering, Faculty of Science and Engineering, The University of Manchester, Manchester M13 9PL, UK
[b] Singapore Center for 3D Printing, School of Mechanical and Aerospace Engineering, Nanyang Technological University, Singapore

HIGHLIGHTS

- The increase of the polymeric molecular weight decreased hydrophilicity, surface hardness, mechanical properties, and crystallinity.
- No significant crystallinity changes were observed during the degradation process.
- Fiber diameter, porosity, and mass loss linearly decreased with the degradation time, while compressive modulus and strength decreased non-linearly.
- Enhanced *in vitro* hADSC proliferation and osteogenic differentiation were observed on lower molecular weight PCL scaffolds.

GRAPHICAL ABSTRACT

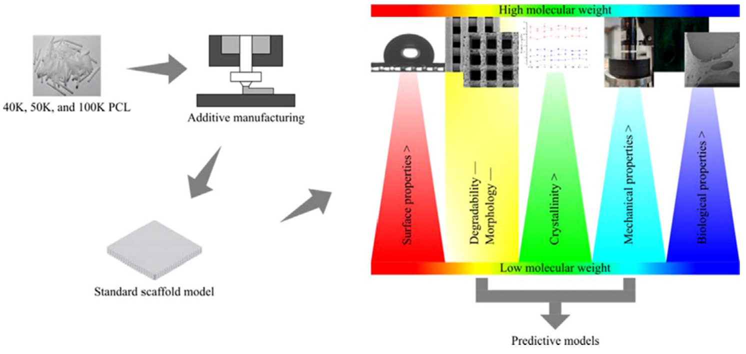

ARTICLE INFO

Article history:
Received 12 November 2021
Revised 5 March 2022
Accepted 22 March 2022
Available online 26 March 2022

Keywords:
3D printing
Biofabrication
Degradation
Polycaprolactone
Scaffolds
Tissue engineering

ABSTRACT

Polycaprolactone (PCL) is one of the most recognized polymeric materials used for bone tissue engineering scaffold fabrication. This study aims to evaluate the effects of the molecular weight (Mn) of PCL on the degradation kinematics, surface, microstructural, thermal, mechanical, and biological properties of 3D printed bone scaffolds. Surface properties were investigated considering water-in-air contact angle and nanoindentation tests, while morphological characteristics and degradation kinematics (accelerated degradation tests) were examined using scanning electron microscopy (SEM), pairing with thermal and mechanical properties monitored at each considered time point. A set of mathematical equations describing the variation of fiber diameter, porosity, mechanical properties, and weight, as a function of molecular weight and degradation time, were obtained based on the experimental results. Human adipose-derived stem cells (hADSCs) proliferation and differentiation tests were also conducted using *in vitro* colorimetric assay. All results indicated that molecular weight had impacts on the surface, mechanical and biological properties of PCL scaffolds, while no significant effects were observed on the degradation rate. Scaffolds with lower molecular weight presented better bio-mechanical properties. These findings provide useful information for the design of polymeric bone tissue engineering scaffolds.

1. Introduction

Scaffolds fabricated through additive manufacturing technology are widely used for bone tissue engineering applications due to the freedom of design, good control over the geometry and

---

* Corresponding authors at: Department of Mechanical, Aerospace and Civil Engineering, School of Engineering, Faculty of Science and Engineering, The University of Manchester, Manchester M13 9PL, UK (P. Bartolo).

E-mail addresses: weiguang.wang@manchester.ac.uk (W. Wang), paulojorge.dasilvabartolo@manchester.ac.uk, pbartolo@ntu.edu.sg (P. Bartolo).

[1] Co-first authors, contribute equally to this work.

https://doi.org/10.1016/j.matdes.2022.110582
0264-1275/

interconnectivity, and high reproducibility [1,2]. A wide range of polymeric (natural and synthetic), ceramic, and composite materials were studied regarding the fabrication of tissue constructs engineering scaffolds. However, synthetic polymeric materials are the most commonly used materials owing to their low immunogenicity and cytotoxicity, easy to process, and the capability to tailor their properties during the polymer synthesis process. Polycaprolactone (PCL) is one of the most relevant synthetic polymers being investigated for bone scaffolds applications due to its mechanical properties and excellent biocompatibility to support cell growth and differentiation, which can ultimately lead to bone tissue regeneration [3–7]. Several studies demonstrated the capability of PCL scaffolds to sustain cell attachment and spreading of stem cells, osteocytes, osteoblasts, chondrocytes, fibroblasts, and endothelial cells [8–13].

The molecular weight of the polymeric materials plays a critical role influencing the properties of both raw materials and fabricated scaffolds. Several studies suggested that high molecular weight polymers may take a longer time to degrade, as longer polymeric chain length require a greater number of ester bonds to be cleaved in order to generate water-soluble monomers/oligomers to allow erosion to proceed [14]. Moreover, some studies also suggested that low molecular weight polymers have a positive effect on angiogenesis stimulation in compression to high molecular weight polymers [15,16], and a similar effect was also reported in terms of cell proliferation and differentiation [17]. When used as biomedical implants, PCL normally undergoes a two-stage degradation process: first hydrolytic degradation through which ester linkages are broken by water, followed by intracellular degradation performed by enzymes [18]. The effect of the degradation process on the crystallinity of PCL scaffolds is not clear with some studies reporting crystallinity changes with the degradation time [19,20], and other studies reporting no changes [21]. Currently, the understanding on how PCL molecular weight's influence on the degradation kinetics is limited, and a systematic study on the effect of PCL molecular weight on the scaffold's biological properties is still required.

Since the polymerization of PCL can be controlled to produce a wide range of molecular weights, a careful choice of PCL molecular weight shows great potential for tuning the biological properties, as well as the capability to bound proteins to suit their pharmacodynamics requirements. This research presents a comprehensive study on the effect of PCL molecular weight on 3D printed scaffold surface properties, degradation kinetics, crystallinity, and mechanical and biological performance of bone tissue engineering scaffolds. Predictive models were also generated based on key results. These results can contribute to the optimal design of bone tissue engineering scaffolds.

2. Materials and methods

2.1. Scaffold design and fabrication

PCL pellets (50,000 number average molecular weight, abbreviated as 50 K PCL; Perstorp, UK) and filaments (40,000 and 100,000 number average molecular weight, abbreviated as 40 K PCL and 100 K PCL; eSun, China) were considered for scaffold fabrication. The density, ρ, of the unprocessed material (UPM) was determined before scaffolds fabrication, as follows:

$$\rho = \frac{m}{V} \tag{1}$$

where, m stands for the mass measured by an analytical balance (LA 214, VMR, USA) and V is the volume measured by the water displacement method at room temperature. Calculated densities of PCL were 1.133 ± 0.006 g/cm^3 for 40 K PCL, 1.124 ± 0.003 g/cm^3 for 50 K PCL, and 1.109 ± 0.008 g/cm^3 for 100 K PCL.

A pellet-based screw-assisted material-extrusion 3D printing system (3D Discovery, regenHU, Switzerland) was considered to fabricate the 50 K PCL scaffolds, while a filament-based material-extrusion additive manufacturing system (i3 Mega S, Anycubic, China) was considered for the fabrication of both the 40 K and 100 K PCL scaffolds. To obtain scaffolds with similar geometric properties, the following processing conditions were considered:

- Pellet-based system: nozzle diameter of 330 μm, melting temperature of 92 °C, layer thickness of 270 μm, deposition velocity of 13 mm/s, and screw rotational velocity of 8 mm/s.
- Filament-based system: nozzle diameter of 300 μm, melting temperature of 95 °C, layer thickness of 270 μm, deposition velocity of 15 mm/s, filament extrusion ratio of 1.3 (40 K PCL) and 1.5 (100 K PCL).

Scaffolds were designed as follows: fiber diameter of 330 μm, pore size of 350 μm, and 0°/90° lay-down pattern. The dimensions of all printed scaffolds were 32 mm × 32 mm × 3.2 mm.

2.2. Surface properties

2.2.1. Wettability

The surface hydrophilicity of the scaffolds was assessed using a KSV CAM 200 system (KSV Instruments, Finland). Briefly, 2 ml of deionized water droplets were thrown down onto the top of the scaffolds through the use of a micrometric liquid dispenser (Hamilton, USA), being the images of the droplets recorded through the use of a DMK 21F04 FireWire monochrome camera (Imaging Source, Germany). The water-in-air contact angle was automatically calculated by using the Attension Theta software (Biolin Scientific, Sweden) according to the sessile drop technique.

2.2.2. Surface hardness and reduced modulus

Nanoindentation tests were used to determine the surface hardness and reduced modulus of the scaffolds. Tests were conducted using an HYSITRON TI 950 TriboIndentor (Bruker, USA) fitted with a standard three-sided pyramidal (Berkovich) probe. A 50 μm spacing was considered between indents with 20 indents for each sample. The nanoindentation was conducted using a load of 5 mN which gives a depth of approximately 2 μm. The load profile was 0.8 μN/s load for 5 s, 2 s hold at peak load (P_{max}) and 0.8 μN/s unload for 5 s. The force and displacements were recorded during the test. The nanoindenter data analysis software HYSITRON TI 950 TriboIndentor (Bruker, USA) was used to estimate the hardness (H) using P_{max} and the contact area (A_c) as follows:

$$H = \frac{P_{max}}{A_c} \tag{2}$$

The reduced modulus (E_r) was calculated using the Oliver-Pharr model considering the contact stiffness (S) and the A_c according to the following equation:

$$E_r = \frac{S \times \sqrt{\pi}}{2 \times \sqrt{A_c}} \tag{3}$$

2.3. In vitro degradation

An accelerated *in vitro* degradation method was considered to evaluate the degradability of all printed scaffolds. Samples were cut into 6 mm × 6 mm × 3.2 mm small blocks, washed and air-dried overnight. Prior to the degradation test (D0), the weight of each scaffold was recorded and then the scaffolds were put into glass vials. 2 ml of 5 M sodium hydroxide solution was added into each vial and all vials were placed in an incubator under standard conditions (5% CO_2, 37 °C, and 95% humidity). The scaffolds were examined every two days. At each time point, samples were removed, rinsed with deionized water three times, and dried in a fume cupboard for 48 h. The scaffolds were then weighed again, and the weight loss of each sample was expressed as a percentage of the original weight, according to the following equation:

$$Mass\ \ loss\ \ (t) = \left(1 - \frac{M(t)}{M_0}\right) \times 100\% \tag{4}$$

where, $M(t)$ is the residual mass of the scaffolds weighted by scale after t days of degradation and M_0 is the initial mass of the scaffolds weighted by scale before degradation. The degradation test stopped when the scaffolds lost their structural integrity. No significant pH value (~13.2) changes were observed during the degradation test.

2.4. Thermal analysis

The crystallinity of the scaffolds was examined using a Q100 Differential Scanning Calorimeter (DSC, TA Instrument, USA). Tests were performed under a nitrogen atmosphere with a flow rate of 50 ml/min.

Two heating cycles and one cooling cycles were conducted during the test. The samples were first heated from −90 °C to 100 °C at the rate of 10 °C/min, followed by fast cooling from 100 °C to −90 °C at the rate of 10 °C/min. The temperature was maintained for 2 min, and the second heating cycle was also conducted from −90 °C to 100 °C at the rate of 10 °C/min. The first heating cycle shows the thermal history after the printing process, presenting the thermal characteristics of the fabricated scaffolds, while the second heating cycle removes the previous thermal history, presenting the intrinsic nature thermal properties of material. The crystallinity (χ_c) was calculated based on the following equation:

$$\chi_c = \frac{\Delta H_m}{\Delta H_m^0} \times \frac{100}{w} \tag{5}$$

where, ΔH_m corresponds to the experimental melting enthalpy, ΔH_m^0 (139.5 J/g) represents the enthalpy of melting of 100% crystalline PCL, and w is the weight fraction of material.

2.5. Morphological characterization

Morphological characterization was performed using scanning electron microscopy (SEM). Scaffold fiber surface and cross-section images were captured using a TESCAN MIRA3 system (TESCAN, Czech), with an accelerating voltage of 2 kV. Before image capturing, the scaffolds were cut into 4 mm blocks and coated with 6 nm of Gold-Palladium (80:20) using the Q150T ES sputter coater (Quorum Technologies, UK). The obtained images were processed by ImageJ (NIH, USA).

2.6. Mechanical characterization

Uniaxial mechanical compression tests were conducted according to the ASTM standards [22,23] with an INSTRON X testing system (High Wycombe, UK) equipped with a 100 N load cell. The scaffolds were cut into 3 mm × 3 mm × 3.24 mm small blocks and the compression tests were performed considering a strain ranging from 0 to 0.3 mm/mm (30%) and a displacement rate of 0.5 mm/min. Compressive modulus and compressive strength were calculated using the software Origin (OriginLab, USA).

2.7. In vitro biological characterization

Human adipose-derived stem cells (hADSCs) (Invitrogen, USA) (passage 3–5) were used for both cell proliferation and differentiation tests. Cells were cultured with MesenPRO RS™ Basal medium (Thermo Fisher Scientific, USA) for proliferation tests and StemPro™ Osteogenesis Differentiation medium (Thermo Fisher Scientific, USA) for differentiation tests. Before cell seeding, scaffolds were trimmed to fit in 48-well plates (Corning, USA), sterilized with 70% ethanol, rinsed with phosphate buffered saline (PBS) (Sigma-Aldrich, UK), and air-dried. Approximately 2×10^4 hADSCs were seeded to each scaffold, and the incubation was conducted under standard conditions.

For cell proliferation, tests were conducted at 1, 3, and 7 days after cell seeding, using the Alamar blue assay. At each time point, cell-seeded samples were first transferred to a new 48-well plate, then adding 0.5 ml medium containing 0.001% Resazurin sodium salt (Sigma-Aldrich, UK). After 4 h of incubation under standard conditions, 150 μL of medium from each well was transferred into a 96-well plate and the fluorescence intensity was measured by biomicroplate reader (BioTec, USA) according to the manufacturer's guidance (540 nm excitation wavelength and 590 nm emission wavelength).

For all cell differentiation tests, hADSCs were first allowed to proliferate for 7 days in Basal medium and then differentiate in osteogenesis differentiation medium for further 7 (corresponding to 14 days of cell culture in the results) and 14 (corresponding to 21 days of cell culture in the results) days. The SensoLYTE® pNPP Alkaline Phosphatase Assay Kit (AnaSpec, Fremont, CA, USA) was used to assess the alkaline phosphatase (ALP) enzymatic activity. On each time point, samples were first rinsed with PBS to remove the culture medium, and then rinsed again with 1× ALP dilution assay buffer. Afterwards, the samples were moved to 15 ml centrifuge tubes, adding 1 ml 1× assay buffer containing 0.2% (v/v%) Triton X-100. To collect the cell lysates, each scaffold was vortexed for 30 s and sonicated for 1 min. The process was repeated twice. Scaffold were then stored under −80 °C for 20 min, using ice crystals to destroy the cell membrane. This procedure was repeated two times. Subsequently, all tubes were centrifuged under 2500*g* for 10 min at 4 °C. Samples were incubated for 1 h at room temperature for the dephosphorylation of p-nitrophenyl phosphate by ALP enzyme, then the supernatants were collected and detected using a microplate reader (405 nm absorbance). ALP concentration was determined based on a standard curve and normalized to the total protein concentration which was evaluated using the bicinchoninic acid assay (Micro BCA Protein Assay Kit, Thermo Fisher Scientific, USA).

Alizarin red-S (ARS) (Sigma-Aldrich, Dorset, UK) was used to determine the mineralization process of hADSCs on the samples. Scaffolds were first washed with PBS to remove the culture medium, and then immersed into 10% neutral formaldehyde solution (Sigma-Aldrich, Dorset, UK) for 15 min. These samples were washed with deionized water and 0.2% ARS staining dye was added to bind the calcium salts (40 min incubation at room temperature). After washing with deionized water to remove residual ARS staining, the samples were then placed into 15 ml centrifuge tubes, with 800 μL 10% acetic acid added, stood for 30 min with gently vibrating, and then heated to 60 °C for 10 min. After being stored into ice for 5 min, all samples were centrifuged under 2500*g* for 15 min. The supernatants were eventually detected by the microplate reader at absorbance of 405 nm.

2.8. Data analysis

At least three scientific repeats ($n \geq 3$) were considered for all experiments, and the data were represented as mean ± standard deviation. One-way ANOVA with Tukey post-hoc tests were applied using the Origin software. The significance levels were set at * $P < 0.05$, ** $P < 0.01$, and *** $P < 0.001$. For degradation, morphological and mechanical characterization, after obtaining all data, results were curve-fitted considering liner and polynomial fitting.

3. Results and discussion

3.1. Material and scaffolds characterization

3.1.1. Surface wettability

The water-in-air contact angle describes the surface wettability and material hydrophilicity, with a contact angle lower than 90° representing a hydrophilic behavior [24,25]. Results showed that the contact angle value increases by increasing the PCL molecular weight (Fig. 1A). This observation can be linked with the surface energy of printed filaments made of PCL with different molecular weights, which is related to the polarity of the molecules [26,27]. Similar results were also reported for other semi-crystalline polymers such as polystyrene [28,29]. However, only 100 K PCL scaffolds showed significant statistical differences in comparison to the other PCL scaffolds, and no significant differences were observed between 40 K and 50 K PCL, probably due to the relatively small molecular weight differences between them.

3.1.2. Nanoindentation

Fig. 1B and 1C show that both surface hardness and reduced modulus significantly decreased by increasing the molecular weight. However, no statistical differences were observed between 50 K PCL and 100 K PCL in terms of reduced modulus (Fig. 1C). The decrease in both cases could be explained by their differences in terms of crystallinity, which is discussed in Section 3.2.1. The scaffolds produced with lower molecular weight PCL presented higher crystallinity, which means the formation of more and larger crystals, enhancing the load-bearing capacity [30].

3.2. In vitro degradation

3.2.1. Thermal analysis with time

The first and second heating curve allows the determine the glass transition temperature (T_g), melting temperature (T_m), melting enthalpy, and crystallinity, while the cooling curve allows to determine the melt crystallization temperature (T_{mc}), crystallization enthalpy (ΔH_c), and crystallinity. Results showed that the crystallinity significantly decreased by increasing the polymer molecular weight (Fig. 2). Similar results were obtained by Jenkins and Harrison [31]. This could be explained by the Hoffman nucleation theory, in which long polymeric chains (higher molecular weight) exhibit longer reptation times, forming loops and cilia that obstruct the reptation processes, leading to lamella thickening [32]. All of these result in lower mobility and crystal growth rate, thereby reducing the final degree of crystallinity [33]. Results also showed that there are no statistical differences in the crystallinity during the degradation time. Full results are available as supplementary material (Tables S1-3).

Further analysis was conducted to study the non-isothermal crystallization kinetics. The relative crystallinity $\chi_c(t)$ can be described as a function of crystallization temperature as follows [34]:

$$\chi_c(t) = \frac{\int_{T_0}^{T} \left(\frac{dH_c}{dT}\right) dT}{\int_{T_0}^{T_\infty} \left(\frac{dH_c}{dT}\right) dT} \tag{6}$$

where, T_0 and T_∞ is the initial and end temperature of crystallization, dH_c is the variation of enthalpy, and dT is the change of temperature. The crystallization time and temperature can be described according to the following equation [35]:

$$t = \frac{T_0 - T}{\varphi} \tag{7}$$

where, T is the temperature at time t. Fig. 3A, 3C, and 3E show the plots of relative crystallinity of 40 K, 50 K, and 100 K PCL versus temperature. Fig. 3B, 3D, and 3F show the plots of relative crystallinity of 40 K, 50 K, and 100 K PCL versus time.

The Avrami equation was considered to describe the crystallization process [36–38]:

$$\chi_c(t) = 1 - e^{-\mathrm{K} \times \mathrm{t}^n} \tag{8}$$

where, $\chi_c(t)$ corresponds to the relative crystallinity (degree of phase conversion), t corresponds to the time of crystallization, K is the Avrami constant related to the nucleation rate and the growth rate, and n is the Avrami exponent related to the type of nucleation and the growth dimension [39]. Taking the logarithms of both sides of Equation (8) gives:

$$\log(-\ln(1 - \chi_c(t))) = n \times \log t + \log K \tag{9}$$

The parameters K and n can be obtained by plotting the $\log(-\ln(1 - \chi_c(t)))$ versus $\log t$ according to the Avrami equation, with n corresponding to the slope and $\log K$ was obtained from the $\log(-\ln(1 - \chi_c(t))$ intercept as shown in Fig. 4.

However, as the DSC tests were conducted under non-isothermal crystallization conditions and the general Avrami equation is not suitable to describe a non-isothermal crystallization process, only the primary stage of the non-isothermal crystallization can be considered [40]. Considering the influence of the cooling rate, Jeziorny modified the Avrami constant K as follows [34]:

$$\log \quad K' = \frac{\log \quad K}{\varphi} \tag{10}$$

where, φ is the cooling rate.

Results showed that in all cases, the Avrami exponents n were close to 2 (Fig. 5), indicating two-dimensional (disk-shaped) nucleation growth. Results also showed that the Avrami constant K' does not depend on the PCL molecular weight (Fig. 5), indicating that the molecular weight of PCL has no significant impact on the growth rates of PCL crystals. However, different trends were observed by Limwanich et al. [41], when investigating the influence of molecular weight on the non-isothermal crystallization of poly(d-lactide). Differences might be attributed to the narrow range of molecular weight considered in this study. The highest/lowest ratio was 4 in the case of poly(d-lactide), while in this study was 2.5. As observed both n value and K' parameters do not change throughout the degradation process (Fig. 5), suggesting well-balanced degradation kinetics of both the amorphous and crystalline regions of PCL.

3.2.2. Morphological characterization with time

Fig. 6 presents the SEM images of scaffolds' top surface and cross-section, with zoom-up fiber surface images in the middle. After printing and before starting the degradation process, the fiber diameter, horizontal pore size, and vertical pore size values were 335.30 ± 6.85 μm, 356.29 ± 8.97 μm, and 160.76 ± 23.99 μm for 40 K PCL scaffolds; 338.23 ± 18.49 μm, 347.84 ± 18.77 μm, and 192.38 ± 26.65 μm for 50 K PCL scaffolds; 333.78 ± 6.40 μm, 350.14 ± 1.83 μm, and 230.42 ± 14.18 μm for 100 K PCL scaffold. These values were closed to the designed values (fiber diameter of 330 μm, horizontal pore size of 350 μm, and vertical pore size of 210 μm), indicating that the extrusion-based additive manufacturing, under the considered processing parameters, is an effective way to produce the designed scaffolds, allowing the fabrication of reproducible scaffolds with relatively stable fiber diameter, pore size, and uniform pore distribution. Minor differences could be attributed to the rheological properties of the polymer melt (viscosity, shear-thinning, and viscoelastic properties) associated with the different molecular weights. Moreover, SEM images after degradation clearly showed the erosion of the fiber caused by hydrolysis. Fig. 7 presents the variation of the average fiber diameter and porosity throughout the degradation time. As observed,

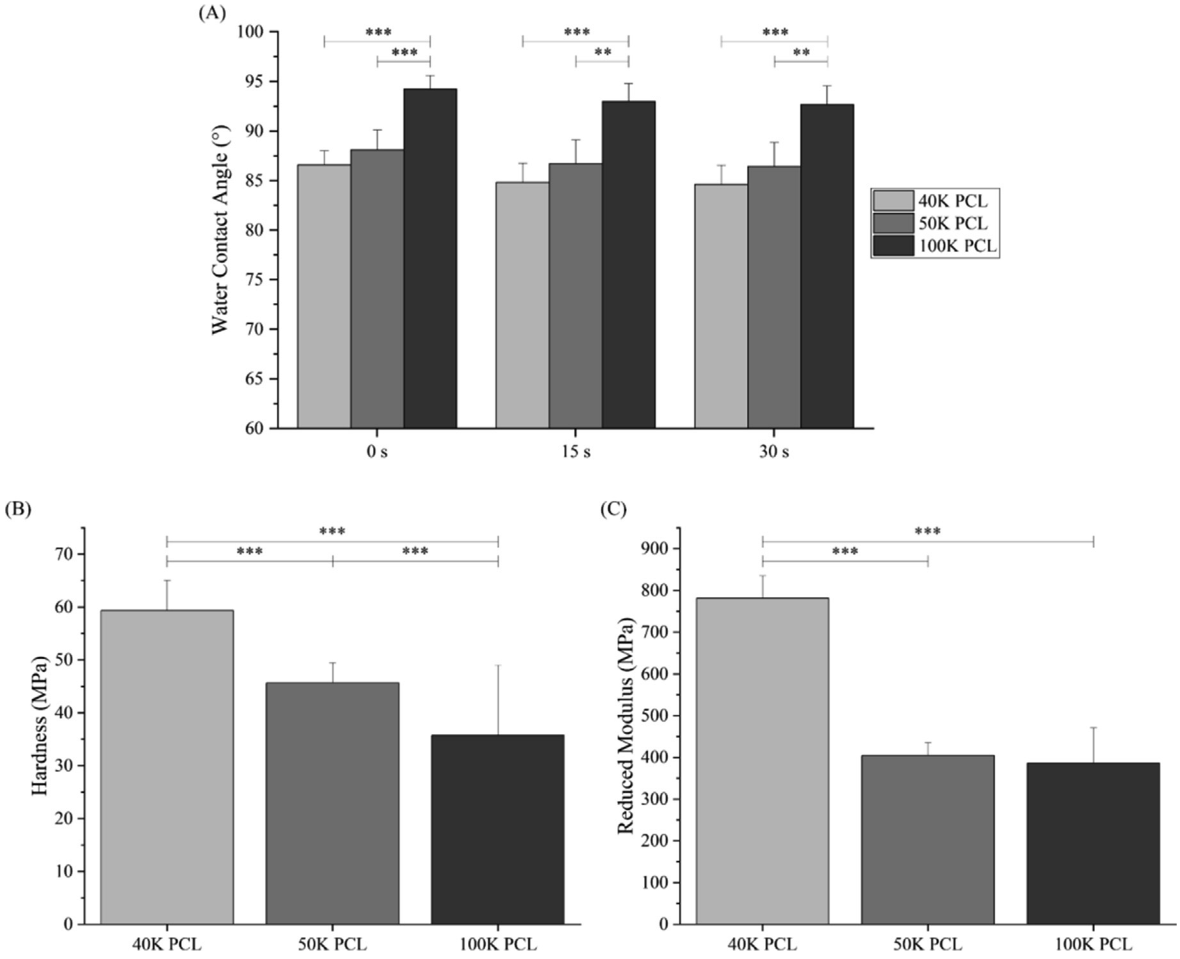

Fig. 1. (A) Water-in-air contact angle, (B) surface hardness, and (C) reduced modulus of 40 K, 50 K, and 100 K PCL scaffolds.

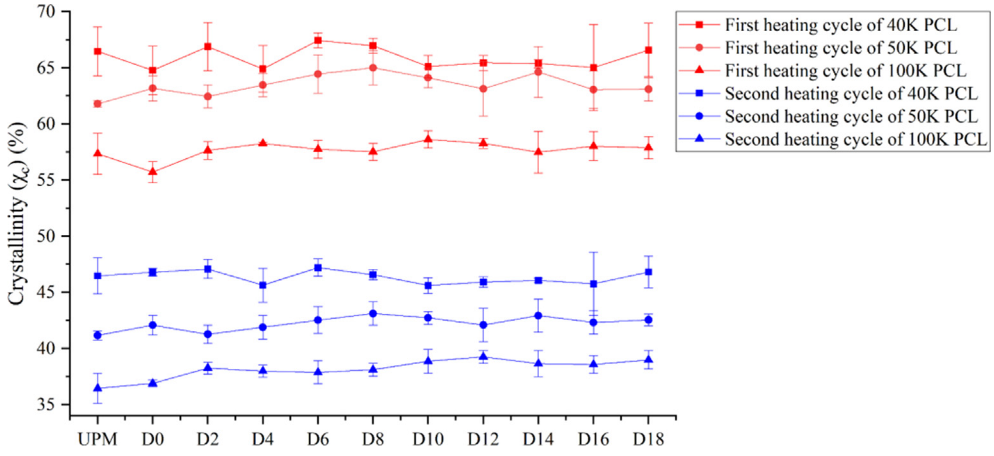

Fig. 2. Crystallinity (heating cycles) variation with time for 40 K, 50 K, and 100 K PCL scaffolds.

both fiber diameter and porosity showed linear-like relationships with time for all considered PCL scaffolds:

$$Fiber\ \ diameter\ \ (t) = F_0 - \beta_f \times t \tag{11}$$

$$Porosity\ \ (t) = P_0 + \beta_p \times t \tag{12}$$

where, F_0 is the filament and P_0 is the porosity before degradation, β_f and β_p are coefficient rates for both fiber diameter and porosity, and t is degradation time expressed in days. Fitting results suggested that the PCL molecular weight has no significant influence on both β_f and β_p (Table 1).

3.2.3. Mass loss with time

The degradation kinetics of PCL scaffolds was determined by measuring the mass loss of the scaffolds over time. Fig. 8 shows that all types of PCL scaffolds exhibit a linear degradation rate described by the following equation:

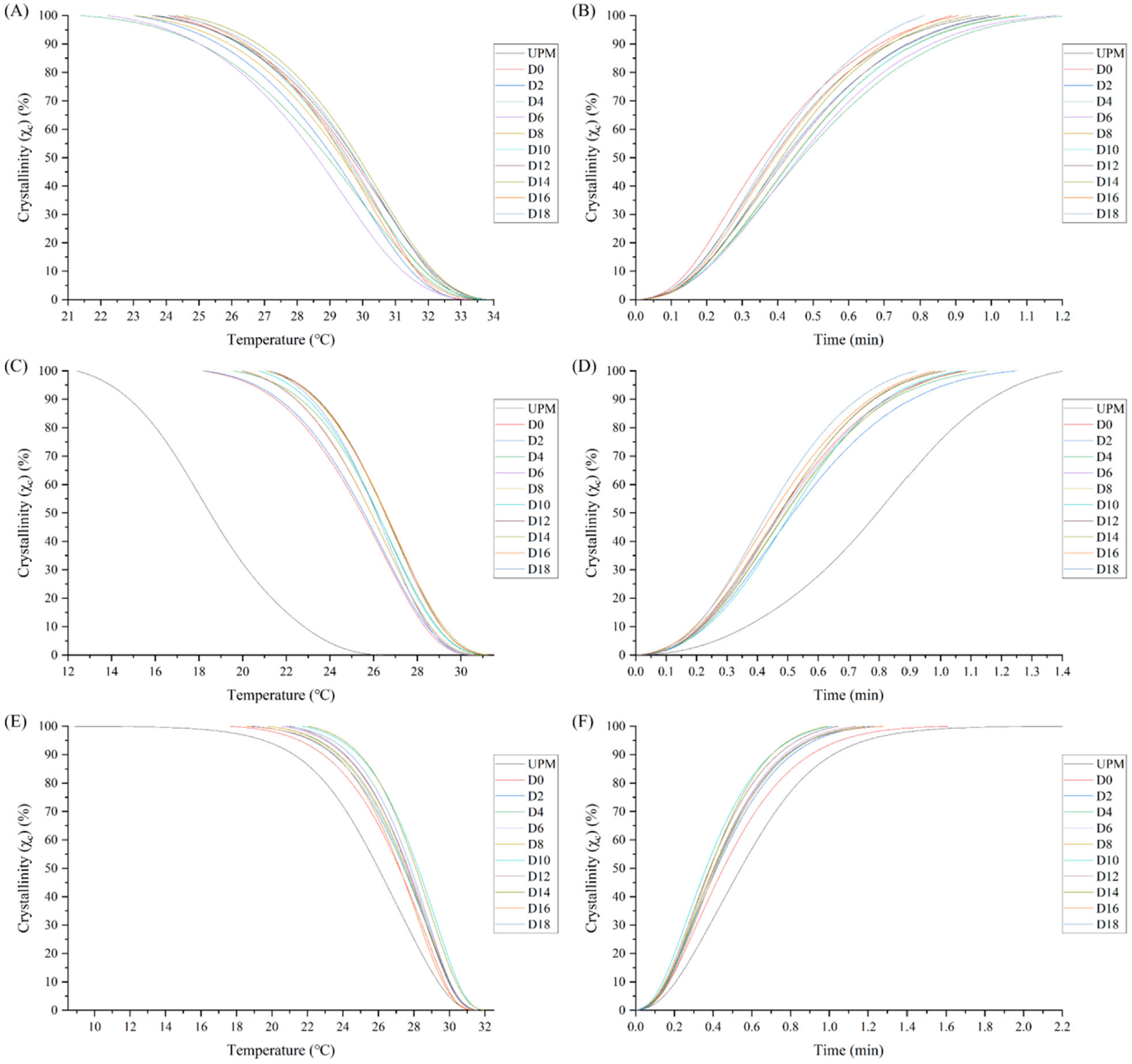

Fig. 3. Relative crystallinity of (A and B) 40 K, (C and D) 50 K, and (E and F) 100 K PCL scaffolds versus (A, C, and E) temperature and (B, D, and F) time.

$$Mass\ \ loss\ \ (t) = \alpha + \beta_m \times t \tag{13}$$

where α is a constant and β_m is the mass loss rate of the scaffolds. Results also showed that the 40 K PCL scaffolds degraded faster in the first 8 days but the degradation process gradually slowed down afterwards. This may be attributed to the fact that the hydrolysis resistance had reached a peak around day 8 [21]. Similar results were also observed in other studies [19,20,42]. However, these results seem to indicate that the degradation rate of PCL scaffolds is not strongly linked with the molecular weight (Table 2). Previous observations were not conclusive on the impact of the molecular weight on the degradation kinetics [14].

Previous research showed that the chain length increases with the molecular weight [14]. For the same type of polymer, a relevant longer chain means that more cleaved ester bonds are required to generate water-soluble monomers/oligomers that allow erosion to proceed, thus leading to a longer degradation time [14]. However, other researchers suggested that the molecular weight has no significant impact on the degradation rate [19]. Furthermore, the hydrophobic material is more difficult to be hydrolyzed, which may partially explain the reason why 100 K PCL (has the highest water contact angle among three molecular weight PCL) degrade slower than the other two groups in the first 8 days.

3.2.4. Mechanical characterization with time

Fig. 8 presents the variation of the compressive modulus and compressive strength over the entire degradation process (day 0 to day 18). The initial compressive modulus of the scaffolds was 104.81 ± 3.49 MPa, 100.35 ± 3.45 MPa, and 61.04 ± 2.36 MPa for 40 K, 50 K, and 100 K PCL scaffolds respectively. The initial compressive strength was 2.85 ± 0.12 MPa, 2.90 ± 0.08 MPa, and 1.55 ± 0.08 MPa for 40 K, 50 K, and 100 K PCL scaffolds respectively. As observed, the fabricated scaffolds have mechanical modulus and strength similar to human trabecular bone, ranging from 50 to 1500 MPa with the mean value of 194 MPa for compressive modulus, and ranging from 1 to 30 MPa with the mean value of 3.55 MPa for compressive strength [43–46]. Results showed that the compressive modulus and compressive strength decreases by increasing the PCL molecular weight. However, no statistical differences were observed between 40 K and 50 K PCL due to the rela-

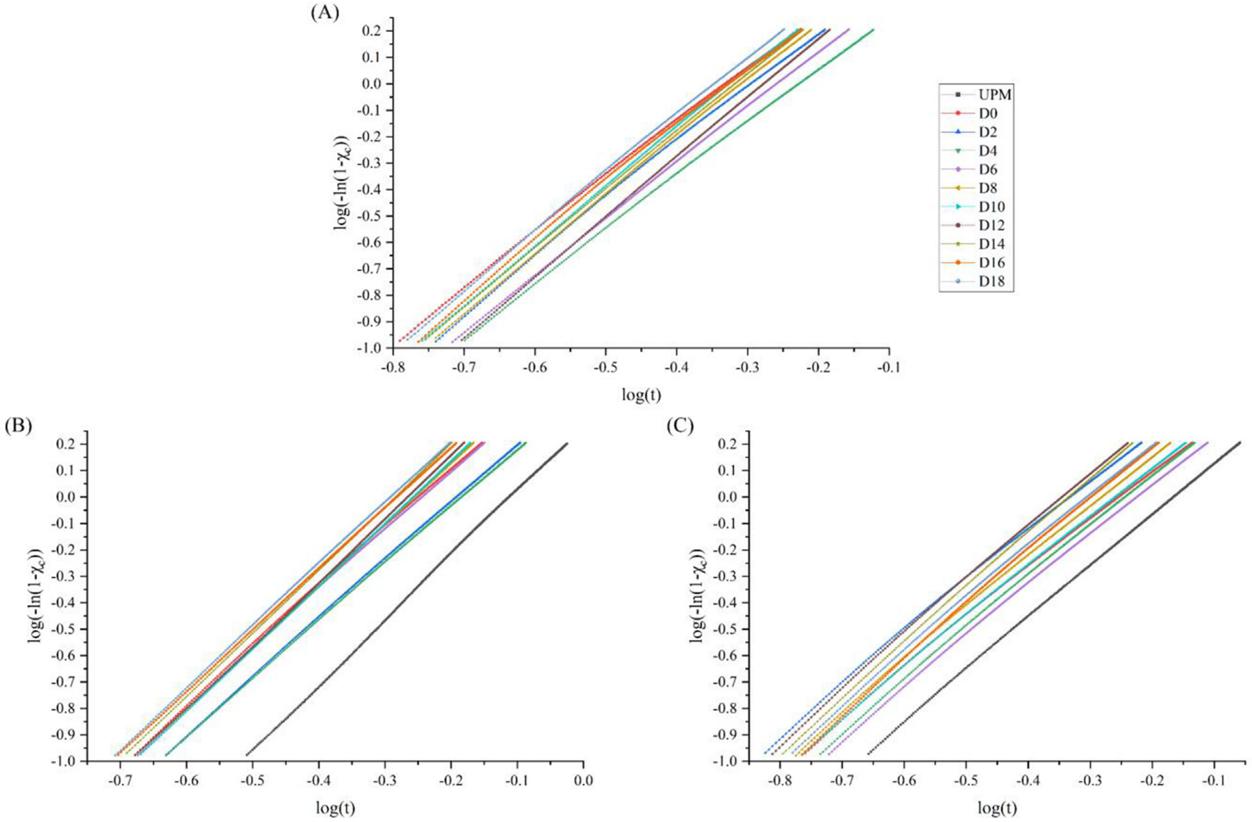

Fig. 4. Avrami plots of (A) 40 K, (B) 50 K, and (C) 100 K PCL scaffolds.

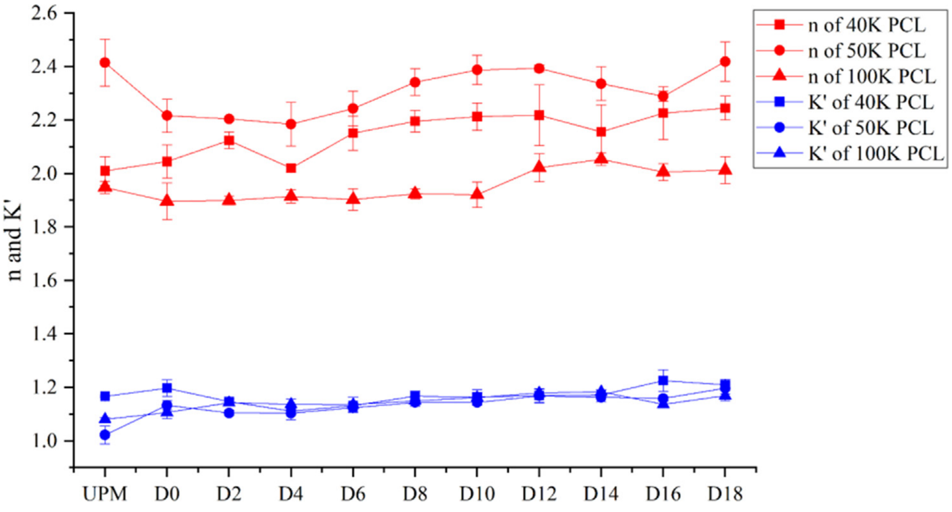

Fig. 5. Crystallization kinetic parameters of the non-isothermal crystallization of 40 K, 50 K, and 100 K PCL scaffolds.

tively small difference in the molecular weight. Furthermore, through the entire degradation process, the 40 K PCL scaffolds exhibit the highest compressive modulus while the 100 K PCL scaffolds exhibit the lowest compressive modulus and compressive strength. Lower molecular weight PCL scaffolds showed higher mechanical properties, which can be attributed to their high crystallinity values. Results also showed that the compressive modulus and compressive strength decreases with time in a non-linear way:

$$Compressive\ modulus\ (Mn, t) = Cm_0(Mn) - \beta_{cm}(Mn) \times t + \gamma_{cm}(Mn) \times t^2 \tag{14}$$

$$Compressive\ strength\ (Mn, t) = Cs_0(Mn) - \beta_{cs}(Mn) \times t + \gamma_{cs}(Mn) \times t^2 \tag{15}$$

where, Cm_0 and Cs_0 corresponds to the compressive modulus and compressive strength before the degradation, β_{cm} and γ_{cm} are the coefficient rates for compressive modulus and compressive strength, β_{cs} and γ_{cs} are the coefficient rates for compressive modulus and compressive strength. The fitted equation parameters are presented in Table 3. Results showed that the coefficients β_{cm}, β_{cs}, and γ_{cm} depend on the PCL molecular weight, being possible to observe that both β_{cm}, β_{cs}, and γ_{cm} varies inversely proportional to

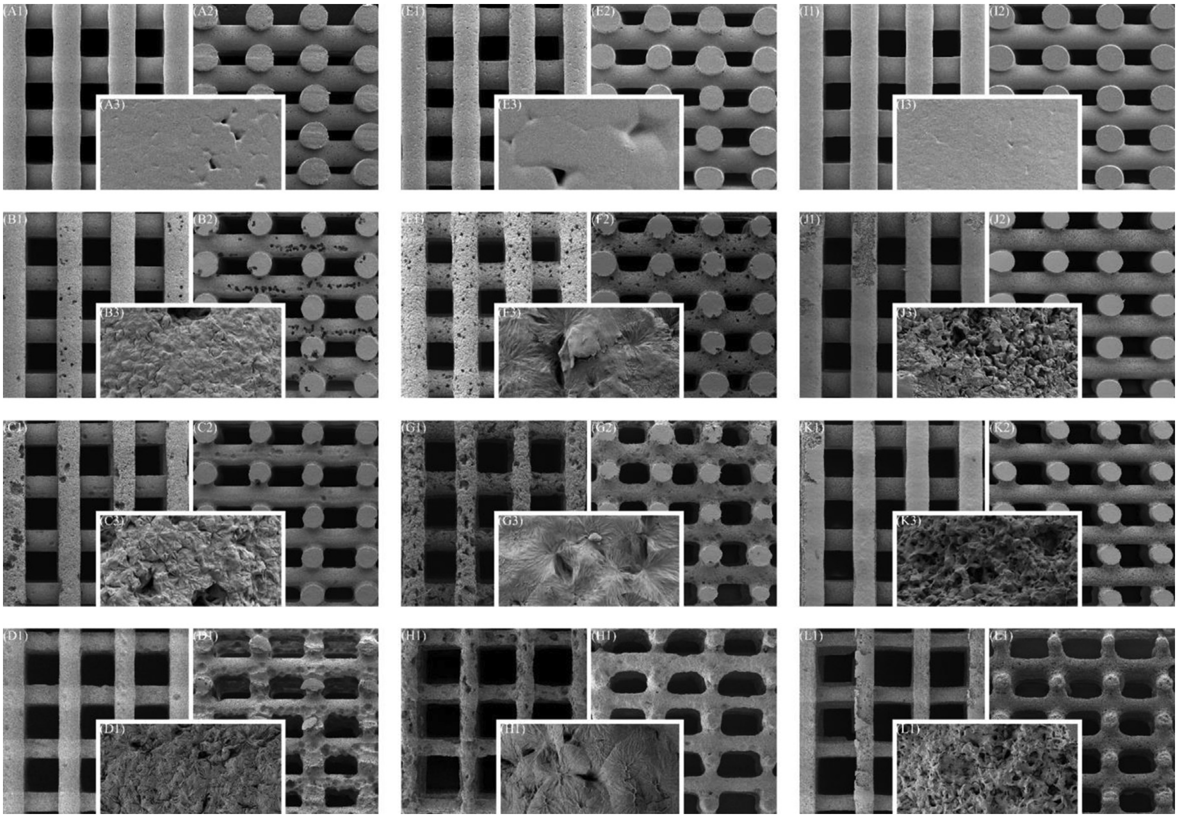

Fig. 6. SEM images of (A-D) 40 K, (E-H) 50 K, and (I-L) 100 K PCL scaffolds at (A, E, and I) D0, (B, F, and J) D6, (C, G, and K) D12, and (D, H, and L) D18 of degradation. (1) Top surface, (2) cross-section, (3) zoom-up fiber surface.

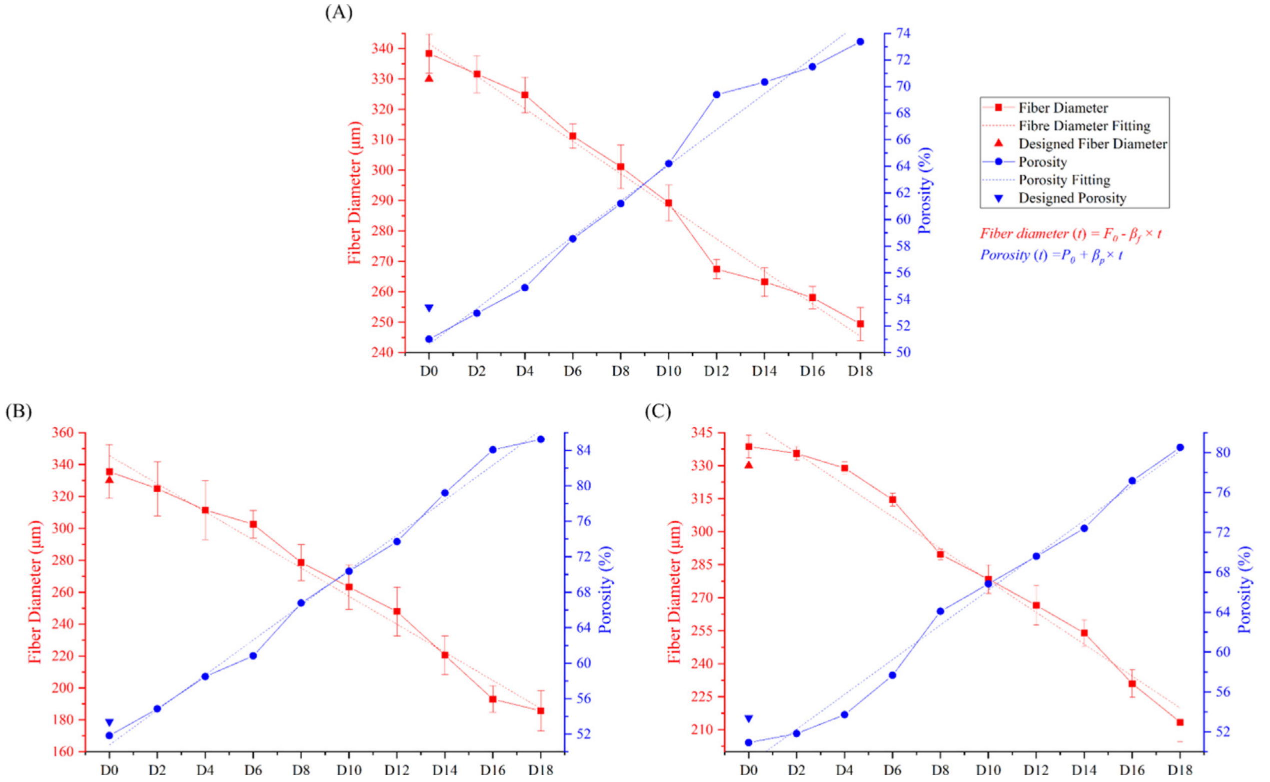

Fig. 7. Fiber diameter (red) and porosity (blue) with time, for (A) 40 K, (B) 50 K, and (C) 100 K PCL scaffolds. (For interpretation of the references to colour in this figure legend, the reader is referred to the web version of this article.)

Table 1
Curve fitting parameters of fiber diameter and porosity for 40 K, 50 K, and 100 K PCL scaffolds.

	Fiber diameter			Porosity		
	F_0	β_f	R^2	P_0	β_p	R^2
40 K PCL	341.6227	5.35032	0.98205	50.63935	1.34523	0.9806
50 K PCL	345.60485	8.80484	0.98239	50.78447	1.97238	0.99251
100 K PCL	350.2371	7.23921	0.98021	48.78181	1.74408	0.9856

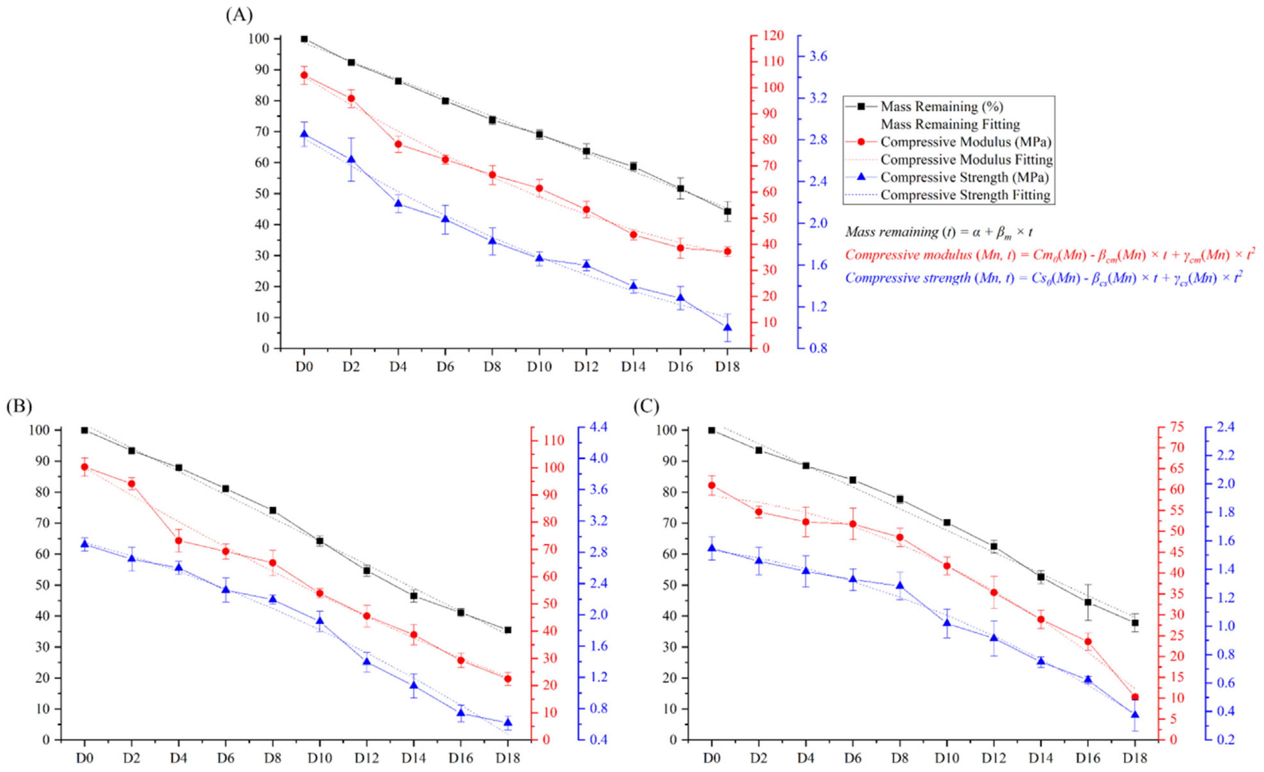

Fig. 8. Mass loss (black), compressive modulus (red), and compressive strength (blue) with time, for (A) 40 K, (B) 50 K, and (C) 100 K PCL scaffolds. (For interpretation of the references to colour in this figure legend, the reader is referred to the web version of this article.)

Table 2
Curve fitting parameters of mass loss for 40 K, 50 K, and 100 K PCL scaffolds.

	α	β_m	R^2
40 K PCL	1.3563	2.96258	0.99707
50 K PCL	−1.74054	3.76536	0.99412
100 K PCL	−2.60251	3.49916	0.98893

the molecular weight. However, there is no direct correlation between γ_{cs} and PCL molecular weight.

3.3. In vitro biological characterization

Cell proliferation results are presented in Fig. 9A. In all cases, the fluorescence intensity increased with time, indicating that all fabricated scaffolds are able to sustain hADSCs proliferation, with no significant cytotoxicity. Among these scaffolds, 40 K PCL scaffolds showed better cell proliferation results, significantly higher than the other two groups. Confocal microscopy images (Fig. 9D) showed cell attachment and distribution after 7 days of proliferation, being possible to observe extensive cell attachment, and spreading along the scaffold filaments.

Fig. 9B shows the ALP activity after 14 and 21 days of cell culture, while Fig. 9C shows the calcium deposition (a typical consequence of osteogenesis) on all types of scaffolds after 14 and 21 days. Results indicated that both ALP activity and calcium deposition significantly increase with time, confirming the capability of all scaffolds to support the hADSCs osteogenic differentiation. Furthermore, on day 21, both ALP protein and calcium deposition increased with the decrease of the PCL molecular weight. The ALP activity and calcium deposition on 40 K PCL scaffolds were also

Table 3
Curve fitting parameters of compressive modulus and compressive strength for 40 K, 50 K, and 100 K PCL scaffolds.

	Compressive modulus				Compressive strength			
	Cm_0	β_{cm}	γ_{cm}	R^2	Cs_0	β_{cs}	γ_{cs}	R^2
40 K PCL	104.17771	5.63844	0.10359	0.98821	2.81451	0.13709	0.00233	0.98451
50 K PCL	99.98364	5.13918	0.04811	0.9867	2.92498	0.08051	−0.00309	0.98664
100 K PCL	58.50677	0.53834	−0.11271	0.98681	1.53473	0.02333	−0.00225	0.99092

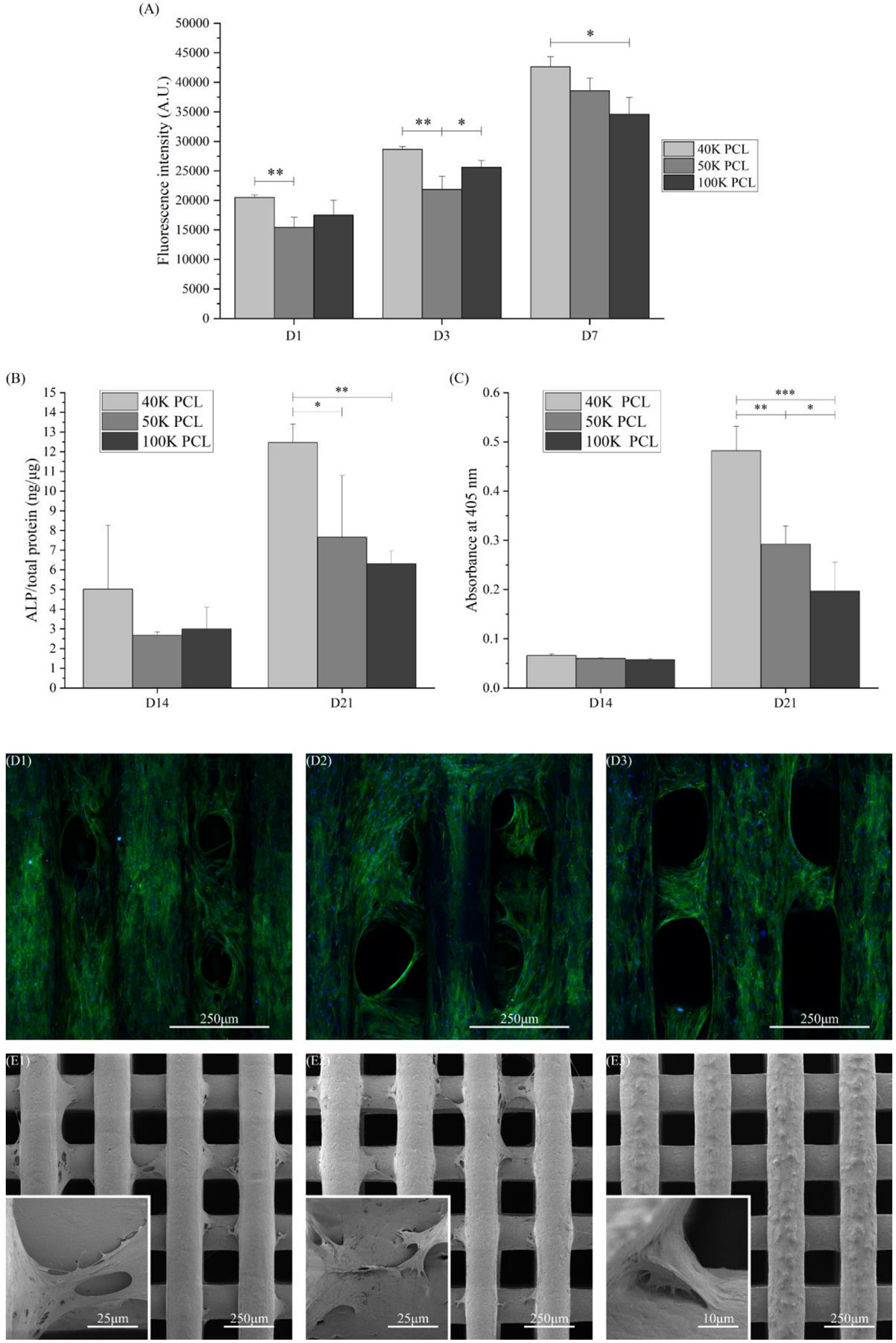

Fig. 9. (A) Viability and proliferation results of hADSCs on 40 K, 50 K, and 100 K PCL scaffolds after 1, 3, and 7 days of cell proliferation. (B). Alkaline phosphatase activity on 40 K, 50 K, and 100 K PCL scaffolds after 14 and 21 days of hADSCs differentiation. (C). Calcium deposition (quantified by Alizarin red-S) on 40 K, 50 K, and 100 K PCL scaffolds after 7, and 14 days of hADSCs differentiation. Confocal microscopy images of (D1) 40 K, (D2) 50 K, and (D3) 100 K PCL scaffolds after 7 days of cell proliferation. SEM images of (E1) 40 K, (E2) 50 K PCL, and (E3) 100 K PCL scaffolds after 21 days of cell differentiation. (For interpretation of the references to colour in this figure legend, the reader is referred to the web version of this article.)

statically higher than the other two groups. This may be attributed to the surface properties of these scaffolds, especially the surface hardness, as the hADSCs osteogenesis is influenced by the substrate surface properties, with stiffer surfaces promoting the osteogenesis process [47,48]. These results could also be associated with the surface wettability of the scaffolds. As previously reported, more hydrophilic surfaces present high proteins adhesion and cell attachment [49–51], which can explain the fact that the most hydrophilic scaffold among the three considered groups presented high cell proliferation and osteogenic differentiation. SEM images (Fig. 9E) showed the cell differentiation results after 21 days, being possible to observe confluent cell sheets bridging through the scaffold fibers.

4. Conclusions

This research investigated the effects of PCL molecular weight on non-biological (surface, degradation, thermal, and mechanical properties) and biological characteristics of bone tissue engineering scaffolds. Results showed a direct impact of the molecular weight on the scaffolds properties. Scaffolds produced with lower molecular weight PCL presented more hydrophilic surfaces, higher surface hardness and better mechanical properties (higher reduced modulus, compressive modulus, and compressive strength), these results also yield to improved cell proliferation and osteogenic differentiation results. However, it was not possible to establish any direct correlation between the degradation rate and the molecular weight, probably due to the narrow range of molecular weight values considered in this study, constrained by the rheological material requirements and printability imposed by the considered additive manufacturing technology. A range of equations describing the variation of fiber diameter, porosity, mechanical properties, and mass loss as a function of degradation time and molecular weight were also established. These equations represent an important contribution to the design of scaffolds, minimizing the need for extensive experimental tests. Once implemented in a Finite Element Analysis simulation tool, they will allow to computer-aided design optimal scaffolds for bone tissue engineering. Longer-term non-accelerated *in vitro* degradation tests will be conducted as well as *in vivo* studies.

Declaration of Competing Interest

The authors declare that they have no known competing financial interests or personal relationships that could have appeared to influence the work reported in this paper.

Acknowledgements

This research was partially supported by Rosetrees & Stoneygate Trust Enterprise Fellowship (Ref: M874) from Rosetrees Trust UK and Stoneygate Trust UK, and the Engineering and Physical Sciences Research Council (EPSRC) UK through the Global Challenges Research Fund (grant number EP/R015139/1).

Appendix A. Supplementary material

Supplementary data to this article can be found online at https://doi.org/10.1016/j.matdes.2022.110582.

References

[1] C. Koski, S. Bose, Effects of amylose content on the mechanical properties of starch-hydroxyapatite 3D printed bone scaffolds, Addit. Manuf. 30 (2019) 100817, https://doi.org/10.1016/j.addma.2019.100817.

[2] N. Sarkar, S. Bose, Controlled release of soy isoflavones from multifunctional 3D printed bone tissue engineering scaffolds, Acta Biomater. 114 (2020) 407–420, https://doi.org/10.1016/j.actbio.2020.07.006.

[3] Y. Hou, W. Wang, P. Bártolo, Novel Poly(ε-caprolactone)/Graphene Scaffolds for Bone Cancer Treatment and Bone Regeneration, 3D Print. Addit. Manuf. 7 (5) (2020) 222–229, https://doi.org/10.1089/3dp.2020.0051.

[4] Z. Meng, J. He, Z. Cai, F. Wang, J. Zhang, L. Wang, R. Ling, D. Li, Design and additive manufacturing of flexible polycaprolactone scaffolds with highly-tunable mechanical properties for soft tissue engineering, Mater. Des. 189 (2020) 108508, https://doi.org/10.1016/j.matdes.2020.108508.

[5] P.R. Lopes Nalesso, W. Wang, Y. Hou, L. Bagne, A.T. Pereira, J.V. Helaehil, T.A. Moretti de Andrade, G.B. Chiarotto, P. Bártolo, G.F. Caetano, In vivo investigation of 3D printed polycaprolactone/graphene electro-active bone scaffolds, Bioprinting 24 (2021) e00164, https://doi.org/10.1016/j.bprint.2021.e00164.

[6] A. Wibowo, C. Vyas, G. Cooper, F. Qulub, R. Suratman, I.A. Mahyuddin, T. Dirgantara, P. Bartolo, 3D Printing of Polycaprolactone-Polyaniline Electroactive Scaffolds for Bone Tissue Engineering, Materials 13 (3) (2020), https://doi.org/10.3390/ma13030512.

[7] H. Liu, Y. Du, G. Yang, X. Hu, L. Wang, B. Liu, J. Wang, S. Zhang, Delivering Proangiogenic Factors from 3D-Printed Polycaprolactone Scaffolds for Vascularized Bone Regeneration, Adv. Healthcare Mater. 9 (23) (2020) 2000727, https://doi.org/10.1002/adhm.v9.2310.1002/adhm.202000727.

[8] N. Naderi, M.F. Griffin, A. Mosahebi, P.E. Butler, A.M. Seifalian, Adipose derived stem cells and platelet rich plasma improve the tissue integration and angiogenesis of biodegradable scaffolds for soft tissue regeneration, Mol. Biol. Rep. 47 (3) (2020) 2005–2013, https://doi.org/10.1007/s11033-020-05297-7.

[9] M. Nieuwoudt, I. Woods, K.F. Eichholz, C. Martins, K. McSweeney, N. Shen, D.A. Hoey, Functionalization of Electrospun Polycaprolactone Scaffolds with Matrix-Binding Osteocyte-Derived Extracellular Vesicles Promotes Osteoblastic Differentiation and Mineralization, Ann. Biomed. Eng. 49 (12) (2021) 3621–3635, https://doi.org/10.1007/s10439-021-02872-2.

[10] N. Abbasi, R.S.B. Lee, S. Ivanovski, R.M. Love, S. Hamlet, In vivo bone regeneration assessment of offset and gradient melt electrowritten (MEW) PCL scaffolds, Biomater. Res. 24 (1) (2020) 17, https://doi.org/10.1186/s40824-020-00196-1.

[11] Manjunath Kamath S., Subha Krishna Rao, Jaison D., Sridhar K., Kasthuri N., Gopinath V., Sivaperumal P., Shantanu Patil S. Melatonin delivery from PCL scaffold enhances glycosaminoglycans deposition in human chondrocytes – Bioactive scaffold model for cartilage regeneration. Process Biochem. 99 (2020) 36–47. https://doi.org/10.1016/j.procbio.2020.08.015.

[12] S. Dikici, F. Claeyssens, S. MacNeil, Pre-Seeding of Simple Electrospun Scaffolds with a Combination of Endothelial Cells and Fibroblasts Strongly Promotes Angiogenesis, Tissue Eng. Regener. Med. 17 (4) (2020) 445–458, https://doi.org/10.1007/s13770-020-00263-7.

[13] A.R. Sadeghi-avalshahr, S. Nokhasteh, A.M. Molavi, N. Mohammad-pour, M. Sadeghi, Tailored PCL Scaffolds as Skin Substitutes Using Sacrificial PVP Fibers and Collagen/Chitosan Blends, Int. J. Mol. Sci. 21 (7) (2020) 2311.

[14] M.A. Woodruff, D.W. Hutmacher, The return of a forgotten polymer—Polycaprolactone in the 21st century, Prog. Polym. Sci. 35 (10) (2010) 1217–1256, https://doi.org/10.1016/j.progpolymsci.2010.04.002.

[15] A.C. Lake, R. Vassy, M. Di Benedetto, D. Lavigne, C. Le Visage, G.Y. Perret, D. Letourneur, Low Molecular Weight Fucoidan Increases VEGF₁₆₅-induced Endothelial Cell Migration by Enhancing VEGF₁₆₅ Binding to VEGFR-2 and NRP1 *, J. Biol. Chem. 281 (49) (2006) 37844–37852, https://doi.org/10.1074/jbc.M600686200.

[16] F. Gao, Y. Liu, Y. He, C. Yang, Y. Wang, X. Shi, G. Wei, Hyaluronan oligosaccharides promote excisional wound healing through enhanced angiogenesis, Matrix Biol. 29 (2) (2010) 107–116, https://doi.org/10.1016/j.matbio.2009.11.002.

[17] N. Zhao, X. Wang, L. Qin, Z. Guo, D. Li, Effect of molecular weight and concentration of hyaluronan on cell proliferation and osteogenic differentiation in vitro, Biochem. Biophys. Res. Commun. 465 (3) (2015) 569–574, https://doi.org/10.1016/j.bbrc.2015.08.061.

[18] S.C. Woodward, P.S. Brewer, F. Moatamed, A. Schindler, C.G. Pitt, The intracellular degradation of poly(ε-caprolactone), J. Biomed. Mater. Res. 19 (4) (1985) 437–444, https://doi.org/10.1002/jbm.820190408.

[19] Q. Ma, K. Shi, T. Su, Z. Wang, Biodegradation of Polycaprolactone (PCL) with Different Molecular Weights by Candida antarctica Lipase, J. Polym. Environ. 28 (11) (2020) 2947–2955, https://doi.org/10.1007/s10924-020-01826-4.

[20] C.G. Pitt, F.I. Chasalow, Y.M. Hibionada, D.M. Klimas, A. Schindler, Aliphatic polyesters. I. The degradation of poly(ϵ-caprolactone) in vivo, J. Appl. Polym. Sci. 26 (11) (1981) 3779–3787, https://doi.org/10.1002/app.1981.070261124.

[21] C.X.F. Lam, M.M. Savalani, S.-H. Teoh, D.W. Hutmacher, Dynamics of in vitro polymer degradation of polycaprolactone-based scaffolds: accelerated versus simulated physiological conditions, Biomed. Mater. 3 (3) (2008) 034108, https://doi.org/10.1088/1748-6041/3/3/034108.

[22] International A, Standard Test Method for Compressive Properties of Rigid Cellular Plastics. ASTM International, West Conshohocken, PA, 2016. https://doi.org/10.1520/D1621-16.

[23] International A, Standard Test Method for Compressive Properties of Rigid Plastics. ASTM International, West Conshohocken, PA. https://doi.org/10.1520/D0695-15.

[24] G. Lamour, A. Hamraoui, A. Buvailo, Y. Xing, S. Keuleyan, V. Prakash, A. Eftekhari-Bafrooei, E. Borguet, Contact Angle Measurements Using a Simplified

Experimental Setup, J. Chem. Educ. 87 (12) (2010) 1403–1407, https://doi.org/10.1021/ed100468u.

[25] C. Dorrer, J. Rühe, Drops on Microstructured Surfaces Coated with Hydrophilic Polymers: Wenzel's Model and Beyond, Langmuir 24 (5) (2008) 1959–1964, https://doi.org/10.1021/la7029938.

[26] M.M. Pereira, K.A. Kurnia, F.L. Sousa, N.J.O. Silva, J.A. Lopes-da-Silva, J.A.P. Coutinho, M.G. Freire, Contact angles and wettability of ionic liquids on polar and non-polar surfaces, PCCP 17 (47) (2015) 31653–31661, https://doi.org/10.1039/c5cp05873b.

[27] N. Giovambattista, P.G. Debenedetti, P.J. Rossky, Effect of Surface Polarity on Water Contact Angle and Interfacial Hydration Structure, J. Phys. Chem. B 111 (32) (2007) 9581–9587, https://doi.org/10.1021/jp071957s.

[28] L. Zhang, J.M. Torkelson, Enhancement of Surface Wettability by Incorporating Polar Initiator Fragments at Chain Ends of Low-Molecular-Weight Polymers, ACS Appl. Mater. Interfaces 9 (14) (2017) 12176–12181, https://doi.org/10.1021/acsami.7b0352510.1021/acsami.7b03525.s001.

[29] Masruroh, T.N. Zahirah, Aulanni'am, S.P. Sakti, D.J.D.H. Santjojo, The effect of molecular weight on the surface wettability of polystyrene treated with nitrogen plasma, IOP Conf. Ser. Mater. Sci. Eng. 432 (2018) 012036, https://doi.org/10.1088/1757-899X/432/1/012036.

[30] F. Song, Q. Wang, T. Wang, The effects of crystallinity on the mechanical properties and the limiting PV (pressure×velocity) value of PTFE, Tribol. Int. 93 (2016) 1–10, https://doi.org/10.1016/j.triboint.2015.09.017.

[31] M.J. Jenkins, K.L. Harrison, The effect of molecular weight on the crystallization kinetics of polycaprolactone, Polym. Adv. Technol. 17 (6) (2006) 474–478, https://doi.org/10.1002/pat.733.

[32] J.D. Hoffman, R.L. Miller, Kinetic of crystallization from the melt and chain folding in polyethylene fractions revisited: theory and experiment, Polymer 38 (13) (1997) 3151–3212, https://doi.org/10.1016/S0032-3861(97)00071-2.

[33] X. Chen, G. Hou, Y. Chen, K. Yang, Y. Dong, H. Zhou, Effect of molecular weight on crystallization, melting behavior and morphology of poly(trimethylene terephalate), Polym. Test. 26 (2) (2007) 144–153, https://doi.org/10.1016/j.polymertesting.2006.08.011.

[34] A. Jeziorny, Parameters characterizing the kinetics of the non-isothermal crystallization of poly(ethylene terephthalate) determined by d.s.c., Polymer 19 (10) (1978) 1142–1144.

[35] Q. Zhang, Z. Zhang, H. Zhang, Z. Mo, Isothermal and nonisothermal crystallization kinetics of nylon-46, J. Polym. Sci., Part B: Polym. Phys. 40 (16) (2002) 1784–1793, https://doi.org/10.1002/polb.10237.

[36] M. Avrami, Kinetics of Phase Change. I General Theory, J. Chem. Phys. 7 (12) (1939) 1103–1112.

[37] M. Avrami, Kinetics of Phase Change. II Transformation-Time Relations for Random Distribution of Nuclei, J. Chem. Phys. 8 (2) (1940) 212–224, https://doi.org/10.1063/1.1750631.

[38] M. Avrami, Granulation, Phase Change, and Microstructure Kinetics of Phase Change III, J. Chem. Phys. 9 (2) (1941) 177–184, https://doi.org/10.1063/1.1750872.

[39] Y.A. Eltahir, H.A.M. Saeed, C. Yuejun, Y. Xia, W. Yimin, Parameters characterizing the kinetics of the non-isothermal crystallization of polyamide 5,6 determined by differential scanning calorimetry, J. Polym. Eng. 34 (4) (2014) 353–358, https://doi.org/10.1515/polyeng-2013-0250.

[40] G.S. Ross, L.J. Frolen, 10. Nucleation and Crystallization, in: R.A. Fava (Ed.), Methods in Experimental Physics, vol. 16, Academic Press, 1980, pp. 339–397, https://doi.org/10.1016/S0076-695X(08)60761-9.

[41] W. Limwanich, S. Phetsuk, P. Meepowpan, N. Kungwan, W. Punyodom, Influence of Molecular Weight on the Non-Isothermal Melt Crystallization of Biodegradable Poly(D-Lactide), Key Eng. Mater. 751 (2017) 221–229, https://doi.org/10.4028/www.scientific.net/KEM.751.221.

[42] Z. Gan, Q. Liang, J. Zhang, X. Jing, Enzymatic degradation of poly(ε-caprolactone) film in phosphate buffer solution containing lipases, Polym. Degrad. Stab. 56 (2) (1997) 209–213, https://doi.org/10.1016/S0141-3910(96)00208-X.

[43] R.C. Thomson, M.J. Yaszemski, J.M. Powers, A.G. Mikos, Fabrication of biodegradable polymer scaffolds to engineer trabecular bone, J. Biomater. Sci. Polym. Ed. 7 (1) (1996) 23–38, https://doi.org/10.1163/156856295X00805.

[44] J.M. Williams, A. Adewunmi, R.M. Schek, C.L. Flanagan, P.H. Krebsbach, S.E. Feinberg, S.J. Hollister, S. Das, Bone tissue engineering using polycaprolactone scaffolds fabricated via selective laser sintering, Biomaterials 26 (23) (2005) 4817–4827, https://doi.org/10.1016/j.biomaterials.2004.11.057.

[45] B.D. Porter, J.B. Oldham, L.S. He, M.E. Zobitz, R.G. Payne, N.K. An, B.L. Currier, G. A. Mikos, M.J. Yaszemski, Mechanical Properties of a Biodegradable Bone Regeneration Scaffold, J. Biomech. Eng. 122 (3) (2000) 286–288, https://doi.org/10.1115/1.429659.

[46] J.C. Lotz, T.N. Gerhart, W.C. Hayes, Mechanical properties of trabecular bone from the proximal femur: A quantitative CT study, J. Comput. Assist. Tomogr. 14 (1) (1990) 107–114, https://doi.org/10.1097/00004728-199001000-00020.

[47] W.C. Clem, S. Chowdhury, S.A. Catledge, J.J. Weimer, F.M. Shaikh, K.M. Hennessy, V.V. Konovalov, M.R. Hill, A. Waterfeld, S.L. Bellis, Y.K. Vohra, Mesenchymal stem cell interaction with ultra-smooth nanostructured diamond for wear-resistant orthopaedic implants, Biomaterials 29 (24–25) (2008) 3461–3468, https://doi.org/10.1016/j.biomaterials.2008.04.045.

[48] M. Franchi, B. Bacchelli, G. Giavaresi, V. De Pasquale, D. Martini, M. Fini, R. Giardino, A. Ruggeri, Influence of Different Implant Surfaces on Peri-Implant Osteogenesis: Histomorphometric Analysis in Sheep, J. Periodontol. 78 (5) (2007) 879–888, https://doi.org/10.1902/jop.2007.060280.

[49] A. Sethuraman, M. Han, R.S. Kane, G. Belfort, Effect of Surface Wettability on the Adhesion of Proteins, Langmuir 20 (18) (2004) 7779–7788, https://doi.org/10.1021/la049454q.

[50] Y. Arima, H. Iwata, Effect of wettability and surface functional groups on protein adsorption and cell adhesion using well-defined mixed self-assembled monolayers, Biomaterials 28 (20) (2007) 3074–3082, https://doi.org/10.1016/j.biomaterials.2007.03.013.

[51] A. Ranella, M. Barberoglou, S. Bakogianni, C. Fotakis, E. Stratakis, Tuning cell adhesion by controlling the roughness and wettability of 3D micro/nano silicon structures, Acta Biomater. 6 (7) (2010) 2711–2720, https://doi.org/10.1016/j.actbio.2010.01.016.